Materials Today Chemistry 53 (2026) 103492

Contents lists available at ScienceDirect

Materials Today Chemistry

journal homepage: www.journals.elsevier.com/materials-today-chemistry/

2,2′-Bithiophene and thieno[3,2-*b*]thiophene-tethered conjugated microporous polymers as organic electrodes for supercapacitor energy storage

Mohamed Gamal Mohamed [a,b,1], Abdul Basit [a,1], Ahmed A.K. Mohammed [b], Shiao-Wei Kuo [a,c,*]

[a] Department of Materials and Optoelectronic Science, Center for Functional Polymers and Supramolecular Materials, National Sun Yat-Sen University, Kaohsiung, 804, Taiwan
[b] Department of Chemistry, Faculty of Science, Assiut University, Assiut, 71516, Egypt
[c] Department of Medicinal and Applied Chemistry, Kaohsiung Medical University, Kaohsiung, 807, Taiwan

ARTICLE INFO

Keywords:
2,2′-Bithiophene
Thieno[3,2-*b*]thiophene
Conjugated microporous polymers
Energy storage
Symmetric coin-cell supercapacitor
Density functional theory

ABSTRACT

Many current supercapacitor (SCs) electrodes still face persistent challenges, including restricted cycle durability, low energy density, and inadequate electrical conductivity. To overcome these drawbacks, conjugated microporous polymers (CMPs) have been proposed as an up-and-coming category of materials stemming from their tunable porosity and extended π-conjugation. In this study, we designed and synthesized two novel CMPs—TPBZ-BTh and TPBZ-TTh—by integrating 1,2,4,5-tetrakis-(4-aminophenyl)benzene (TPBZ-4NH_2) with 2,2′-Bithiophene-5,5′-dicarboxaldehyde [BTh–2CHO], and thieno[3,2-*b*]thiophene-2,5-dicarbaldehyde [TTh-2CHO] units through a [4 + 2] condensation Schiff-base reaction. Both CMPs exhibited outstanding thermal stability, well-developed porous structures, and efficient charge-transport pathways, all of which are crucial for improving electrochemical properties. Among these two, TPBZ-TTh CMP demonstrated a remarkable specific capacitance of 536 F g^{-1} [1 A g^{-1}] and sustaining 96.6% capacitance retention even after prolonged cycling, reflecting its excellent stability and reversibility. To further evaluate its practical potential, a symmetric coin-cell supercapacitor was fabricated using TPBZ-TTh CMP material. The symmetric coin cell achieved the specific capacitance of 207 F g^{-1} (recorded at 1 A g^{-1}), alongside impressive power and energy densities, confirming its viability for real-world SCS applications. These findings underscore the power of rational design of CMPs frameworks with BTh and TTh for next-generation high-performance, durable, and sustainable supercapacitor materials.

1. Introduction

With the rapid expansion of digital technologies, global energy demand continues to rise as electronic devices become integral to daily life. However, this digital expansion brings profound challenges—chief among them, the generation, storage, and sustainable supply of the energy required to maintain such a connected lifestyle. Presently, global energy consumption relies heavily on a combination of renewable resources (such as wind, solar, ocean, and biomass) and non-renewable sources (including coal and oil) [1–3]. The global energy crisis stems from the widening gap between the stagnant or limited energy supply and the escalating demand driven by population growth, industrialization, and technological advancement. A central challenge of modern civilization lies in achieving a delicate equilibrium—balancing environmental sustainability with the convenience and efficiency expected by consumers, while maintaining a stable and reliable energy infrastructure to sustain economic growth [4–10]. Energy storage technologies play a pivotal role. Among them, batteries and supercapacitors (SCs) have gained widespread attention for their capability to store and deliver energy efficiently. While batteries, especially lithium-ion

* Corresponding author. Department of Materials and Optoelectronic Science, Center for Functional Polymers and Supramolecular Materials, National Sun Yat-Sen University, Kaohsiung, 804, Taiwan.
E-mail address: kuosw@faculty.nsysu.edu.tw (S.-W. Kuo).
[1] These authors contributed equally to this work.

https://doi.org/10.1016/j.mtchem.2026.103492
Received 18 November 2025; Received in revised form 8 February 2026; Accepted 3 March 2026
Available online 9 March 2026

batteries (LIBs)—are celebrated for their high energy densities, their operation is often constrained by slow redox reactions, limited cycle lifespans, and safety concerns such as thermal runaway. They also suffer from high manufacturing costs and dependence on scarce, environmentally damaging raw materials [11–16].

Porous organic polymers (POPs) have attracted considerable attention owing to their distinctive structural elegance, lightweight yet robust carbon-rich frameworks, and exceptionally high surface areas coupled with tunable pore architectures. These unique features enable POPs to perform a critical role in energy conversion and storage machinery [17–20]. Their versatile chemical design allows for exceptional stability under harsh environmental conditions, seamless integration of redox-active or ion-conductive sites, and precise control over ion diffusion pathways, all of which are essential for optimizing electrochemical performance [21]. An additional advantage of POPs lies in their sustainable synthesis. These materials can be constructed from readily available and renewable organic precursors, offering an eco-friendly alternative to conventional lithium-based technologies that suffer from resource scarcity, high production costs, and uneven geographical distribution of lithium deposits [22,23]. By harnessing abundant organic feedstocks, POP-based systems not only alleviate concerns related to resource depletion but also advance greener, more sustainable strategies for the growth of next-generation energy storage systems. Thanks to their large surface area, thermal stability, porosity, and versatile functionality, POPs have been widely applied in areas such as energy storage, optoelectronics, gas adsorption and separation, and heterogeneous catalysis [24–29]. POPs are categorized into subclasses: covalent organic frameworks (COFs), CMPs, and hyper-crosslinked polymers (HCPs), [27–32]. Among these families, CMPs stand out due to the synergistic combination of extended π-conjugation and intrinsic microporosity. This rare interplay enables CMPs to serve as a versatile molecular platform that bridges the gap between electronic conductivity and structural porosity [33,34]. The conjugated backbones of CMPs promote efficient charge delocalization, a property rarely found in conventional porous materials, while their microporous nature ensures a high ion-accessible surface area crucial for rapid charge transport [35]. This dual advantage, combined with their remarkable chemical resilience, thermal stability, and tunable electronic structure, positions CMPs as ideal candidates for a broad spectrum of advanced energy technologies. In particular, the interconnected π-conjugated networks facilitate rapid ion diffusion and high-rate charge discharge processes, making these materials highly effective for supercapacitors, lithium–sulfur batteries, and sodium-ion storage devices [13,26]. The strategic incorporation of heteroatoms and redox-active sites into the framework of CMPs has significantly broadened their functional scope [34].

Tetraphenylbenzene (TPBZ) is an aromatic organic compound in which four phenyl groups are attached to a central benzene ring. Its rigid and highly conjugated framework provides excellent structural stability and strong π–π stacking interactions. Owing to its symmetric and bulky architecture, TPBZ is widely employed as a versatile building block for constructing POPs with promising applications in artificial photosynthesis and wastewater treatment [36,37]. Among the various building blocks for constructing advanced CMPs, sulfur-containing heterocyclic compounds, particularly 2,2′-Bithiophene (BTh) and Thieno[3,2-*b*] thiophene (TTh), have garnered immense attention in recent years. Their unique π-conjugated frameworks and electroactive sulfur heteroatoms endow them with outstanding electrical and electrochemical properties, thus making them perfect for applications involving advanced energy storage [38–40]. Structurally, both compounds contain thiophene rings, yet they differ in configuration: bithiophene consists of two thiophene units linearly connected through a carbon–carbon bond, while dithiophene features a more intricate linkage that influences its conjugation and electronic delocalization characteristics. These thiophene (Th)-based units are particularly advantageous for supercapacitor electrode materials, as their conjugated backbones facilitate efficient charge transport, while their sulfur atoms participate in reversible redox reactions, enhancing both capacitance and stability. Moreover, their intrinsic chemical robustness and structural resilience allow them to withstand repeated charge–discharge cycles without significant degradation, maintaining excellent cycling durability [41–44]. While various CMPs have been evaluated as SC electrodes, those constructed from BTh and TTh building blocks have yet to be systematically assessed for electrochemical performance.

In this study, we successfully synthesized a series of TPBZ-based CMPs [TPBZ-BTh and TPBZ-TTh CMPs] and systematically evaluated their electrochemical performance. The results underscore the remarkable potential of functionalized TPBZ-based CMP frameworks as highly efficient electrode materials for organic supercapacitor systems. The TPBZ backbone serves as a structurally robust and π-conjugated framework, capable of forming moderate surface-area porous architectures. By strategically integrating TPBZ units with BTh and TTh moieties, we developed electrode materials exhibiting superior electrical conductivity, enhanced charge-transfer efficiency, and significantly improved specific capacitance. TPBZ-TTh CMP shows excellent stability and electrochemical performance, delivering a high specific capacitance of 536 F g^{-1} at 1 A g^{-1} with 96.6% retention after long-term cycling. When applied in a symmetric coin-cell, it achieved a specific capacitance of 207 F g^{-1}, demonstrating strong practical potential for energy storage applications.

2. Experimental section

2.1. Materials

1,4-dioxane (DO), 1,2,4,5-tetrabromobenzene (TBBZ), mesitylene, 4-aminophenylboronic acid (BZB-NH_2, 98%), thieno[3,2-*b*]thiophene-2,5-dicarbaldehyde [TTh-2CHO], 2,2′-Bithiophene-5,5′-dicarboxaldehyde [BTh–2CHO], anhydrous magnesium sulphate ($MgSO_4$, ≥99.5%), tetrakis(triphenylphosphine)palladium [$Pd(PPh_3)_4$, 98%], potassium carbonate (K_2CO_3, ≥99.8%), tetrahydrofuran (THF), and acetone, were supplied by Sigma-Aldrich and Alfa Aesar, respectively.

2.2. Synthesis of TPBZ-4NH_2

In a dry, nitrogen-purged round-bottom flask, TBBZ (0.7 g), BZB-NH_2 (2.13 g), $Pd(PPh_3)_4$ (105 mg), and potassium carbonate (K_2CO_3, 2.5 g, 18.09 mmol) were introduced as reactants. The reaction vessel was evacuated for 20 min to thoroughly remove residual air and moisture, ensuring an oxygen- and moisture-free environment conducive to effective cross-coupling. Subsequently, 1,4-dioxane (40 mL) and deionized water (8 mL) were added as the solvent system. The reaction mixture was heated to 110 °C with continuous stirring for three days under inert atmospheric conditions, allowing complete progression of the Suzuki–Miyaura cross-coupling reaction. After the finishing point of the reaction, the mixture was naturally cooled to ambient temperature. Subsequently, 150 mL of H_2O was introduced, which triggered the precipitation of the crude product from the reaction medium. To get rid of any inorganic salts, leftover catalyst, and unreacted boronic acid, the solid product was gathered using vacuum filtering and extensively cleaned with more deionized water. The crude material obtained was further refined through column chromatography, employing a 1:1 solvent mixture of dichloromethane and tetrahydrofuran as the eluent. This purification step yielded the target compound TPBZ-4NH_2 as a light-colored solid in 0.77 g (yield: 88%, Scheme S1).

2.3. Preparation of TPBZ-BTh and TPBZ-TTh CMPs

A mixture containing TPBZ-4NH_2 (0.10 g), BTh–2CHO (0.05 g), or TTh-2CHO (0.04 g) was prepared in individual 25 mL Schlenk tubes. To each tube, a solvent mixture of mesitylene (5 mL) and 1,4-dioxane (5 mL) was added, followed by 1 mL of 6 M acetic acid as the catalyst. The reaction mixtures were then degassed via three freeze–pump–thaw

cycles to eliminate any dissolved oxygen and moisture, ensuring an inert environment conducive to effective polymerization. After degassing, the tubes were flame-sealed under vacuum to maintain an oxygen-free atmosphere. The sealed reaction tubes were subsequently heated to 110 °C and maintained at this temperature for three days, allowing the Schiff-base condensation reaction to proceed to completion. After the reaction mixtures were finished and allowed to cool to an ambient temperature, the solid products were collected using vacuum filtering. The obtained solids were thoroughly washed in sequence with DMF, tetrahydrofuran (THF), and acetone to remove any unreacted monomers, oligomers, or residual catalysts. Finally, the purified materials were dried under vacuum at 100 °C overnight, yielding the desired TPBZ-BTh CMP as a yellow color and TPBZ-TTh CMP as a dark brown color.

3. Results and discussion

3.1. Structural and Physicochemical characterization of TPBZ-BTh and TPBZ-TTh CMPs

Two novel thiophene (Th)-based conjugated microporous polymers (CMPs) were successfully synthesized by incorporating two thiophene-derived dialdehyde monomers—[2,2']bithiophenyl-5,5′-dicarbaldehyde (BTh-2CHO) and thieno[3,2-*b*]thiophene-2,5-dicarbaldehyde (TTh-2CHO)—into a TPBZ-4NH_2 precursor through a catalyst-free Schiff-base condensation reaction [4 + 2 type], as shown in Fig. 1(a) and (b). The TPBZ-4NH_2 precursor was obtained through a Suzuki coupling reaction involving TBBZ and TPBZ-4NH_2, as detailed in the experimental section. Nuclear magnetic resonance (NMR) and Fourier-transform infrared (FT-IR) spectroscopic techniques indisputably validated the successful synthesis of TPBZ-4NH_2 as a building unit. The FT-IR spectrum of TPBZ-4NH_2 (Fig. S1) displayed prominent absorption vibrations at 3431 cm^{-1} and 3352 cm^{-1}, corresponding to N–H stretching bands of amino (NH_2) groups, verifying the presence of free amine functionalities. Further absorption vibrations observed at 3039 cm^{-1} and 1631 cm^{-1} were attributed to aromatic C–H stretching and C═C stretching bands, respectively. ^{1}H NMR spectrum of TPBZ-4NH_2 (Fig. S2) exhibited four distinct proton resonances at 7.1, 6.8, 6.4, and 5.0 ppm, which were assigned to the aromatic protons and NH_2 protons, respectively. Furthermore, the ^{13}C NMR spectrum of TPBZ-4NH_2 (Fig. S3) revealed well-defined signals within the 146.8–113.4 ppm region, characteristic of aromatic carbon environments. The production of highly crosslinked polymer networks was clearly confirmed by the complete insolubility of both TPBZ-BTh and TPBZ-TTh CMPs in all common organic solvents, including DMF, THF, DMSO, acetone, and ethanol. This insolubility behavior is a hallmark of successful network formation through complete imine (C═N) linkage condensation, signifying a rigid conjugated framework with excellent structural integrity and chemical resistance. The chemical structures of TPBZ-BTh and TPBZ-TTh CMPs were verified by FT-IR and cross-polarization magic-angle spinning (CPMAS) ^{13}C NMR spectroscopy. The FT-IR spectra [Fig. 1(c)] exhibited distinct absorption bands corresponding to aromatic C–H stretching (3026–3034 cm^{-1}), C═N (1667 cm^{-1}), aromatic C═C stretching (1647–1599 cm^{-1}), and C–S (710 cm^{-1}). The absence of characteristic peaks corresponding to the C═O and CHO functional groups in the FTIR spectra of TPBZ-BTh and TPBZ-TTh CMPs confirms the complete consumption of these groups during [4 + 2]

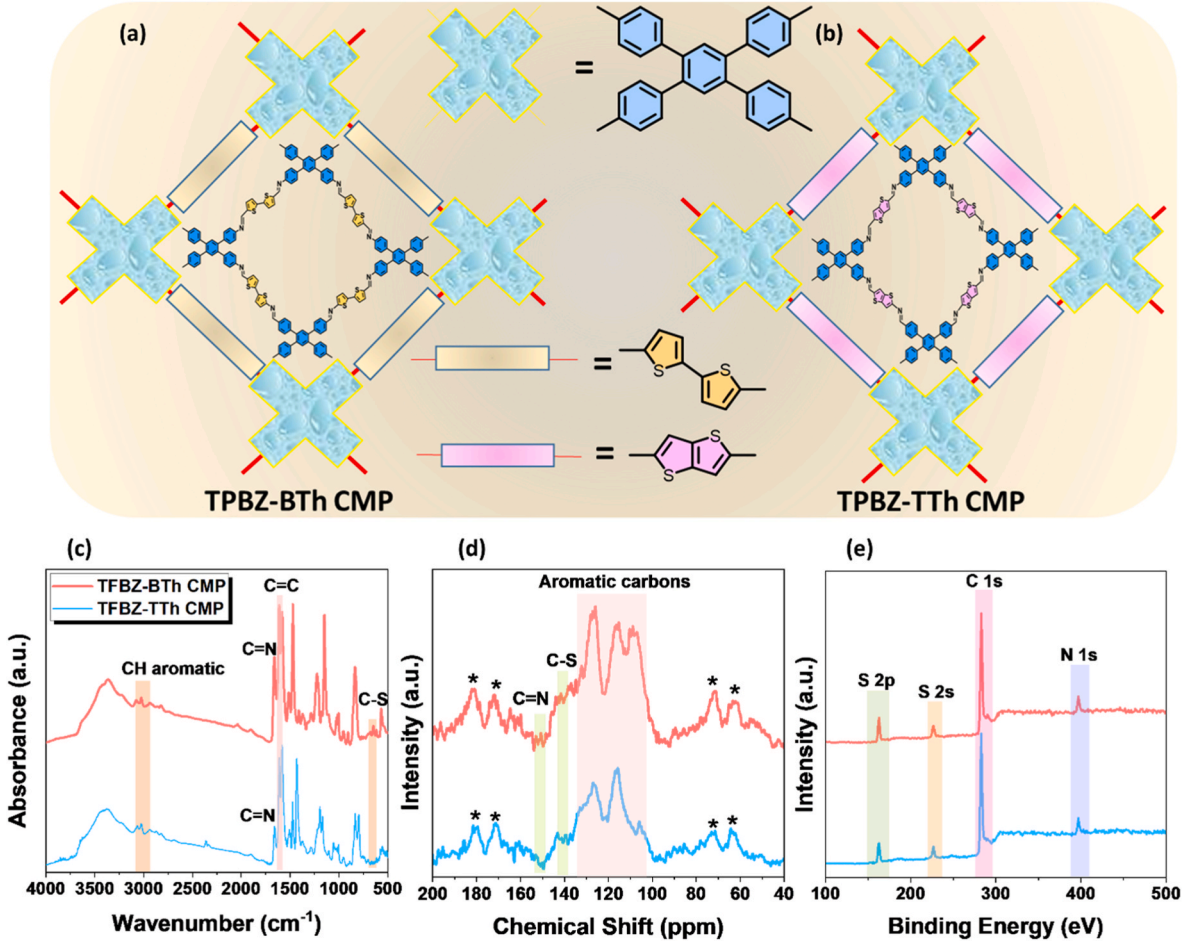

Fig. 1. Schematic illustration of (a) TPBZ-BTh and (b) TPBZ-TTh CMPs, (c) FTIR spectra, (d) solid-state ^{13}C NMR spectra [* is the side band of solid-state NMR.], and (e) XPS spectra of TPBZ-BTh and TPBZ-TTh CMPs.

polymerization [45,46]. The CPMAS ^{13}C NMR spectra [Fig. 1(d)] further supported the formation of the imine-linked networks, displaying resonances in the approximately 151 ppm region (C═N carbons) and 140–104 ppm region (C–S and aromatic carbons), characteristic of conjugated frameworks containing imine linkages and aromatic rings [46,47]. X-ray photoelectron spectroscopy (XPS) gave thorough explanations of the fundamental components and chemical properties of the frameworks. The survey spectra [Fig. 1(e)] show the existence of C, N, and S, consistent with the designed structure. The atomic compositions (Table S1) were 73.0 % C, 10.8 % N, and 16.1 % S for TPBZ-BTh CMP, and 75.8 % C, 9.5 % N, and 14.6 % S for TPBZ-TTh CMP. The high-resolution X-ray photoelectron spectroscopy (XPS) spectra of the synthesized TPBZ-BTh and TPBZ-TTh CMPs [Fig. 2(a–f)] provided detailed insights into the chemical bonding atmospheres of the constituent elements. For the C 1s spectra, TPBZ-BTh CMP [Fig. 2(a)] exhibited distinguishing peaks at 283.1 eV and 282.4 eV, which were assigned to C–C/C═C bonds within the aromatic framework and C–N/C═N bonds arising from the imine linkages, respectively. Similarly, TPBZ-TTh CMP [Fig. 2(d)] displayed corresponding peaks at 282.8 eV (C–C/C═C) and 282.3 eV (C–N/C═N), confirming the preservation of the conjugated backbone and successful imine formation. Additional weak signals appearing at 284.4 eV for TPBZ-BTh CMP and 283.8 eV for TPBZ-TTh CMP were attributed to C–S bonding, verifying the incorporation of Th moieties into the polymer networks. The N 1s spectra further corroborated these findings, showing two well-resolved peaks at 396.8 eV corresponding to C═N, and 398.4 eV for C–N for TPBZ-BTh CMP [Fig. 2(b)], while TPBZ-TTh CMP [Fig. 2(e)] exhibited similar features at 396.7 eV associated with C═N and 397.9 eV for C–N. The S 2p spectra of both TPBZ-BTh and TPBZ-TTh CMPs displayed characteristic spin–orbit doublets at 162.2/163.4 eV for TPBZ-BTh CMP [Fig. 2(c)] and 162.1/163.3 eV for TPBZ-TTh CMP [Fig. 2(f)], associated with the components of S $2p_{3/2}$ and S $2p_{1/2}$ of thiophene sulfur atoms [48–50].

The relative proportion of each functional group was further quantified by calculating the absolute area of the fitted peaks (Table S2). This detailed analysis confirms the successful incorporation and chemical state of the key elements within both TPBZ-CMPs. Thermogravimetric analysis (TGA) revealed remarkable heat stability for both CMPs [Fig. 3 (a)]. The 10% weight loss temperatures (T_{d10}) were 537 °C for TPBZ-BTh CMP and 611 °C for TPBZ-TTh CMP. The char yields at 800 °C were 71.6% and 78.2%, respectively. The enhanced stability of TPBZ-TTh CMP can be attributed to the higher conjugation and rigidity introduced by the TTh backbone. X-ray diffraction (XRD) patterns [Fig. 3(b)] exhibited broad halos centered around $2\theta \approx 19.5°$, which is attributed to localized π–π stacking between aromatic segments, confirming the amorphous nature of both TPBZ-BTh and TPBZ-TTh CMPs. The absence of sharp peaks indicates a non-crystalline framework, which is advantageous for electrochemical applications. Amorphous materials often possess abundant coordinatively unsaturated sites and open-shell defect

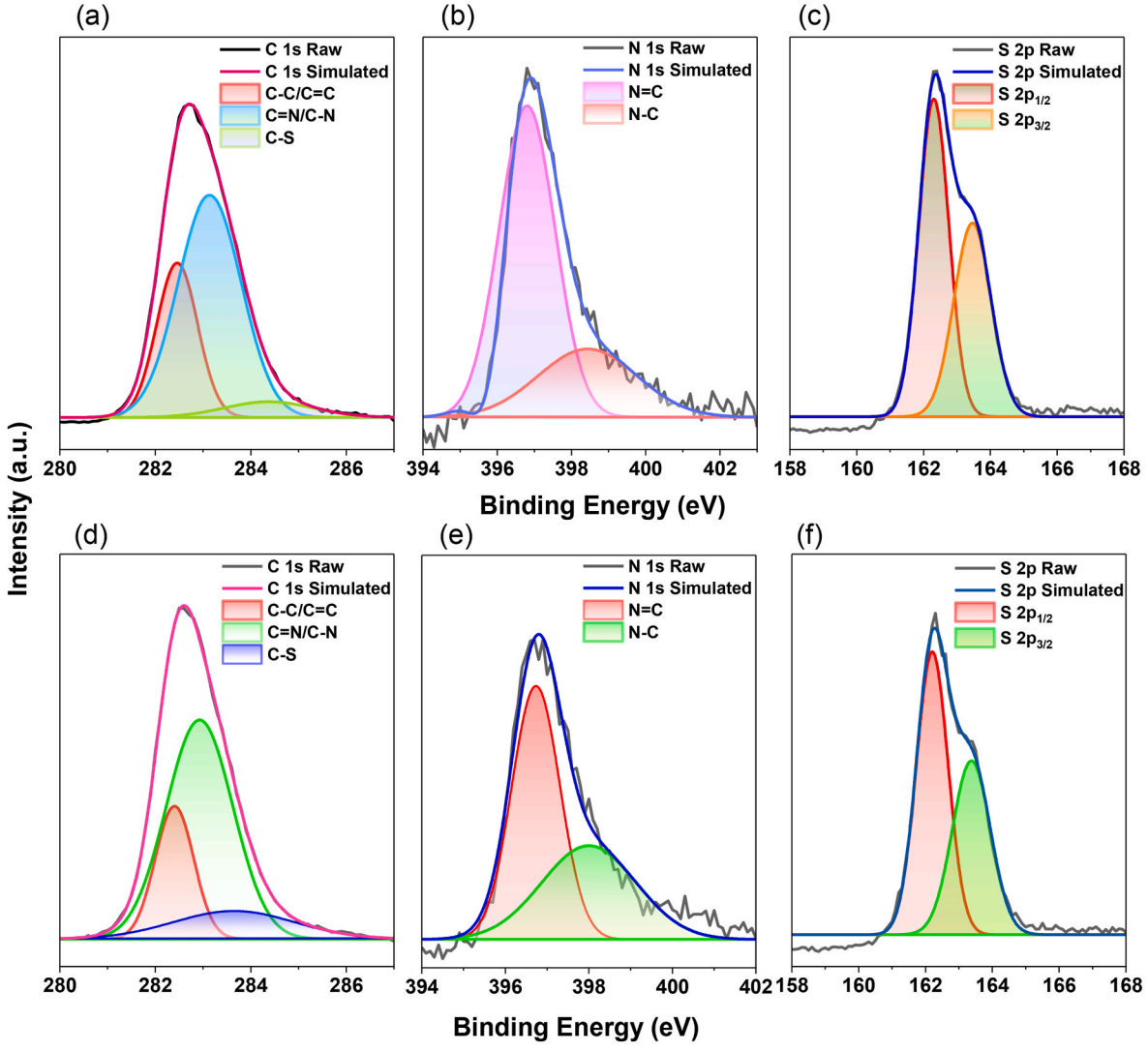

Fig. 2. (a-f) Deconvolution XPS profiles of the C 1s (a, d) and N 1s (b, e) and S 2p (c, f) for (a-c) TPBZ-BTh CMP and (d-f) TPBZ-TTh CMP.

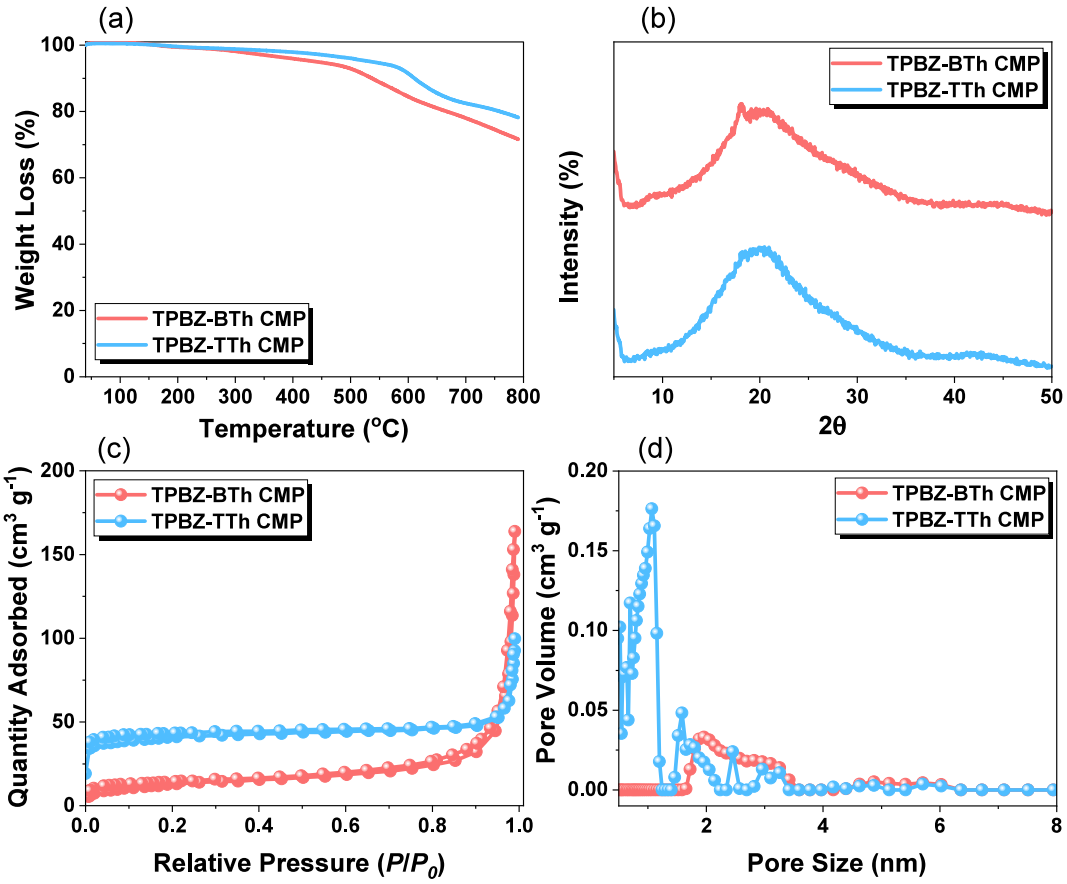

Fig. 3. (a) TGA traces, (b) XRD profiles, (c) N_2 adsorption-desorption isotherms, and (d) pore size diameters profiles of TPBZ-BTh and TPBZ-TTh CMP.

states, providing active centers for electrochemical reactions. Moreover, their structural disorder promotes efficient ion diffusion and charge transfer, thus enhancing long-term cycling stability [51]. The porous features of the produced TPBZ-based CMPs were comprehensively studied by nitrogen (N_2) adsorption–desorption isotherm measurements. Surface area (S_{BET}) and total pore volume (TPV) were determined based on the Brunauer–Emmett–Teller (BET) method and the Non-Local Density Functional Theory (NLDFT) model. As depicted in Fig. 3(c), both TPBZ-BTh and TPBZ-TTh CMP had Type II isotherms, characteristic of microporous materials. Quantitatively, TPBZ-BTh CMP possessed S_{BET} of 47 $m^2\ g^{-1}$ and a TPV of 0.24 $cm^3\ g^{-1}$, whereas TPBZ-TTh CMP demonstrated a substantially higher S_{BET} of 126 $m^2\ g^{-1}$ and a TPV of 0.14 $cm^3\ g^{-1}$. The arrangement of pore sizes further revealed that TPBZ-BTh CMP contained pores predominantly in the 1.02–2.5 nm range, while TPBZ-TTh CMP featured narrower pores centered around 1.98 nm [Fig. 3(d)]. The difference in the BET surface area of TPBZ-TTh CMP and TPBZ-BTh CMP mainly arises from the structural rigidity of the thiophene-based linkers. TPBZ-TTh CMP contains a rigid, planar fused thieno[3,2-*b*]thiophene (TTh) unit, which limits backbone twisting and promotes stable, accessible micropore formation. In contrast, the flexible bithiophene (BTh) linker in TPBZ-BTh CMP allows greater chain rotation, leading to partial pore collapse and lower accessible surface area.

Scanning electron microscopy (SEM) images [Fig. 4(a–f)] revealed that both TPBZ-BTh and TPBZ-TTh CMPs consist of irregular agglomerates of amorphous particles. Elemental mapping via SEM-EDS confirmed the homogeneous distribution of C (violet), N (green), and S (red) across the TPBZ-BTh and TPBZ-TTh CMPs [Fig. 4(g-l)], verifying compositional uniformity. Transmission electron microscopy (TEM) images of TPBZ-BTh and TPBZ-TTh CMPs (Fig. S4) further illustrated disordered, non-crystalline morphologies, devoid of any lattice fringes, even at high magnification.

3.2. *The electrochemical properties of TPBZ-BTh and TPBZ-TTh CMPs were studied using a three-electrode configuration*

The electrochemical behavior of the synthesized TPBZ-BTh and TPBZ-TTh CMPs was methodically examined through CV and GCD measurements. These techniques provided detailed insights into their charge storage competence along with general electrochemical performance. Electrochemical measurements were carried out in a three-electrode system with TPBZ-BTh and TPBZ-TTh CMPs-coated electrodes as the working electrode, Hg/HgO as the reference, Pt wire as the counter electrode, and 1 M KOH electrolyte. The CV curves of TPBZ-BTh and TPBZ-TTh CMPs, collected from −1.0 to 0.0 V at 5–20 mV s^{-1} [Fig. 5 (a) and (b)], revealed quasi-rectangular shapes, a hallmark of electric double-layer capacitance (EDLC) behavior. However, the lack of noticeable redox peaks at all scan rates indicates that the charge storage process is mainly controlled by electrostatic ion adsorption occurring at the interface of the electrolyte and the electrode. Nevertheless, the slight distortion from an ideal rectangular profile suggests a minor pseudocapacitive contribution, likely arising from surface heteroatoms (N and S) capable of reversible faradaic reactions [52,53]. In agreement with the CV findings, the GCD curves [Fig. 5(c) and (d)] for both TPBZ-BTh and TPBZ-TTh CMPs exhibited well-defined symmetrical and nearly triangular shapes. This observation further verifies that their charge storage behavior is predominantly governed by EDLC, with only minor contributions from pseudocapacitive processes. The GCD tests were performed over a current density range of 1–20 A g^{-1} within an identical potential range (−1.0 to 0.0 V). Notably, TPBZ-TTh CMP exhibited longer discharge times than TPBZ-BTh CMP at all current densities, signifying a higher charge storage capability. This enhancement can be

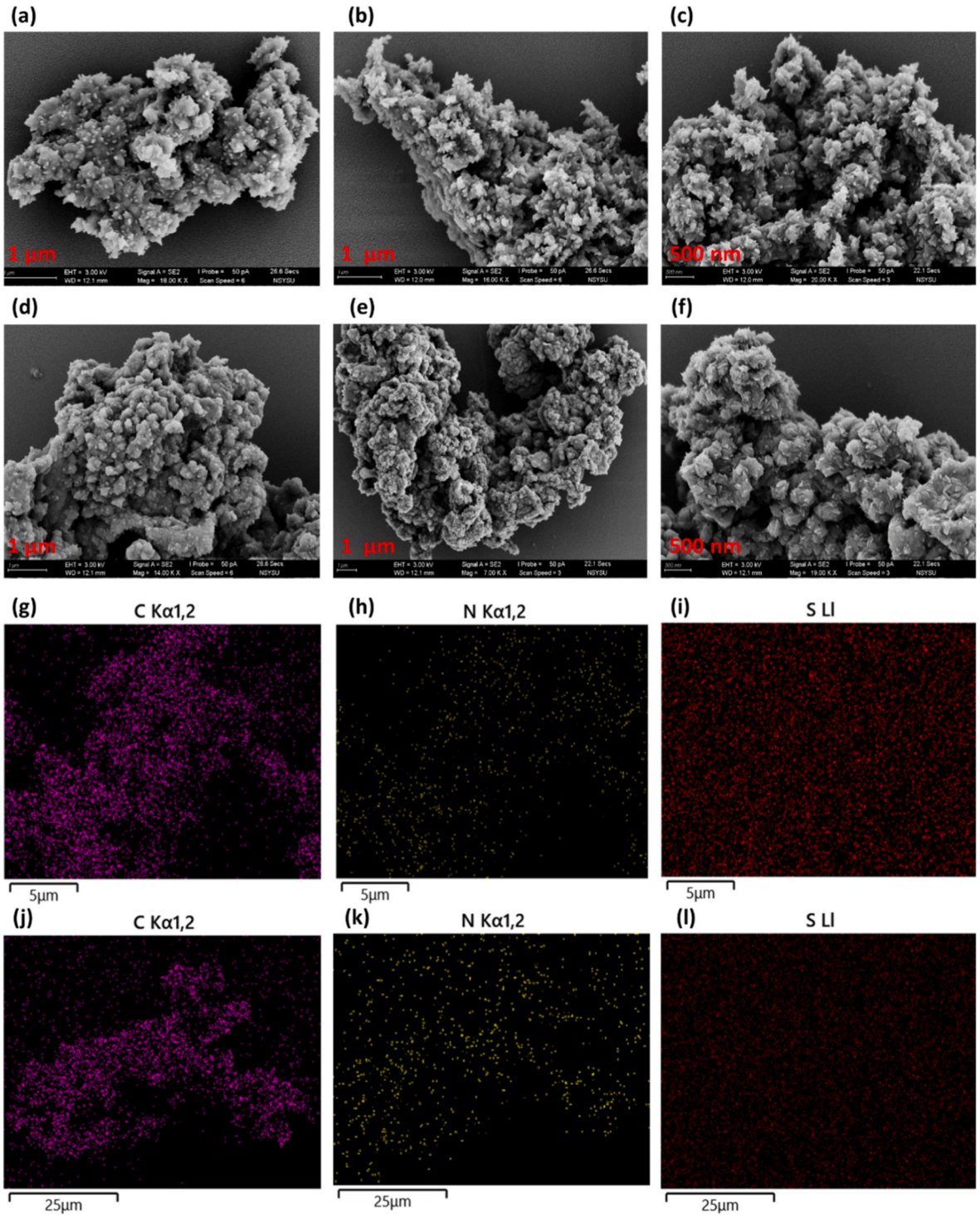

Fig. 4. (a-f) SEM images and (g-l) SEM-EDS images of (a-c, g-i) TPBZ-BTh CMP and (d-f, j-l) TPBZ-TTh CMP.

ascribed to the greater surface area, tighter microporous structure, and more efficient ion diffusion pathways. At lower current densities, the electrolyte ions could fully access the internal micropores, resulting in maximized utilization of active sites and enhanced specific capacitance.

In contrast, at higher applied current densities, the shortened ion diffusion time restricted charge storage primarily to the outer surface of the material, leading to a reduction in capacitance. This phenomenon highlights the influence of ion transport limitations at elevated charge–discharge rates [51]. The pseudocapacitive and EDLC contributions were also separated using Trasatti's technique. A semi-infinite diffusion process is confirmed by a linear relationship seen in the plot of the square root of scan rate ($v^{0.5}$) against the reciprocal of areal capacitance (C^{-1}) [Fig. 6(a)].

Equation (1) defines the converse of EDLC as the y-intercept of this linear fit, which makes it possible to quantitatively distinguish between diffusion-controlled and capacitive charge storage components. The y-intercept associated with this linear fit is attributed to the reciprocal of the total capacitance (C_t^{-1}), as described by Equation (1):

$$C^{-1} = constant \times v^{\frac{1}{2}} + Ct^{-1} \quad (1)$$

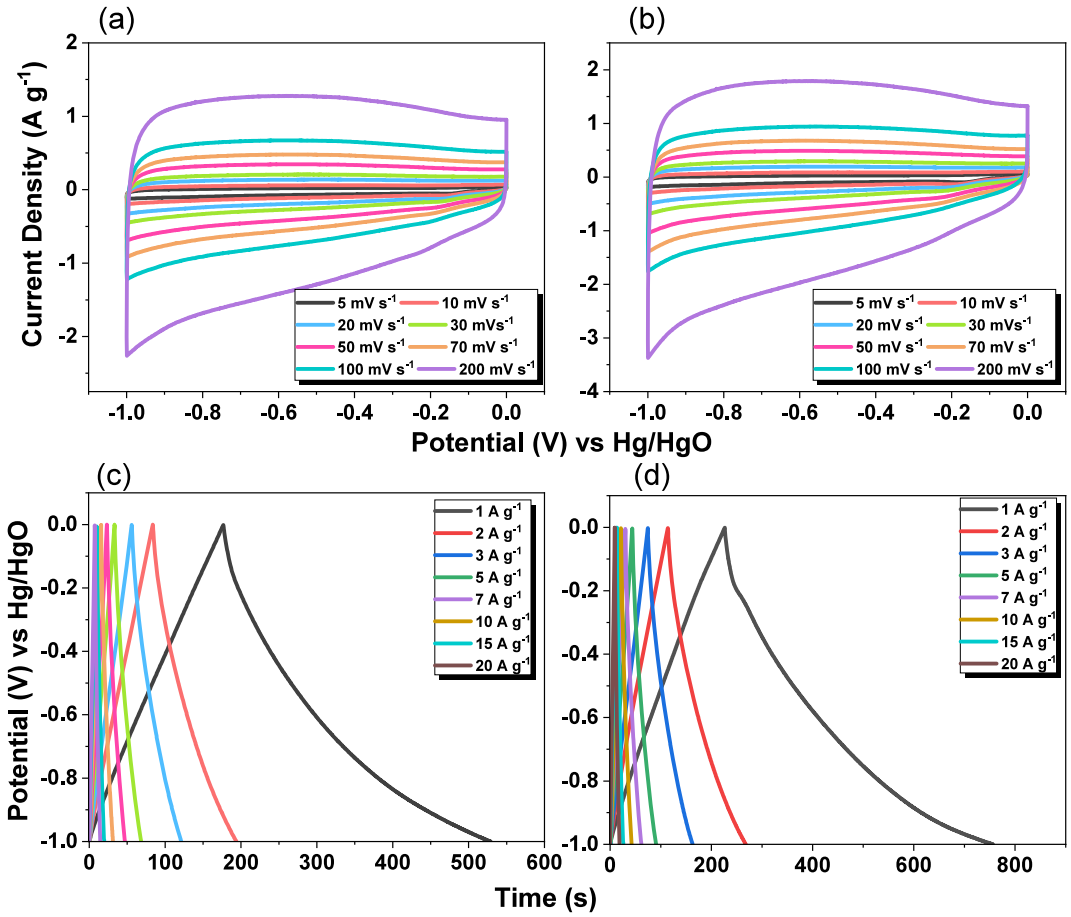

Fig. 5. (a, b) Cyclic voltammetry (CV) and (c, d) galvanostatic Charge-discharge (GCD) curves of (a, c) TPBZ-BTh CMP and (b, d) TPBZ-TTh CMP, measured employing a three-electrode cell.

The analysis derived from Trasatti's method further corroborates the charge-storage mechanism of the TPBZ-based CMP electrodes. Considering semi-infinite ion diffusion kinetics, plotting C against the reciprocal of $v^{-0.5}$ likewise reveals a linear connection. A trustworthy indicator of the inherent electrochemical behavior is the interception of this linear fit, which is equal to the inverse of C_t. As anticipated, with increasing scan rates, insufficient time for electrolyte ions to penetrate the porous structure enhances the capacitive contribution. The total capacitance (C_t) and proportional offerings of the diffusion- and surface-controlled processes were computed using this connection. Fig. 6(c) and (d), revealed that the EDLC (surface-controlled) contribution was found to be 10% for TPBZ-BTh CMP and only 8% for TPBZ-TTh CMP at 5 mV s^{-1}. At lower scan speeds, however, the pseudocapacitive contribution increases, which is brought on by sulfur heteroatoms embedded in the dithiophene moieties, enabling more complete usage of active sites and deeper ion penetration. The long-term electrochemical stability of the TPBZ-based CMPs was evaluated through continuous GCD cycling over 5000 consecutive cycles. As illustrated in Fig. 7(a), both TPBZ-BTh and TPBZ-TTh CMPs exhibited remarkable cycling stability and excellent capacitance retention. After 5000 cycles, TPBZ-BTh and TPBZ-TTh CMP retained 92.2% and 96.6%, respectively, of their initial capacitance values. The complementary advantages of the BTh and TTh units are responsible for these materials' greater stability, which enhances electrical conductivity and chemical stability of the polymer network. The presence of heteroatoms (N and S) within the conjugated framework further contributes to performance enhancement by introducing additional redox-active sites, facilitating charge delocalization, and stabilizing the electrochemical interface during cycling. These structural and compositional advantages collectively result in enhanced charge-storage capacity, minimized degradation, and long-term operational reliability of the TPBZ-CMP electrodes [54]. From the GCD data, the specific capacitances were calculated to be 536 F g^{-1} for TPBZ-TTh and 358 F g^{-1} for TPBZ-BTh CMPs at a current density of 1 A g^{-1}.

Due to limited ion diffusion and inadequate time for electrolyte ions to reach all active sites within the electrode material, specific capacitance gradually decreases with increasing current density, as depicted in Fig. 7(b). Electrochemical impedance spectroscopy (EIS) was employed to study deeper into charge storage kinetics and interfacial properties of the electrode materials. The EIS data were fitted using a standard equivalent circuit model (Fig. S5) consisting of a solution resistance (Rs), a charge-transfer resistance (R_{ct}), a constant phase element (CPE) representing non-ideal EDLC, and a Warburg element (W) associated with ion diffusion. The Nyquist plots of TPBZ-BTh and TPBZ-TTh CMPs [Fig. 7(c)], at high frequencies, show that the semicircular feature corresponds to the R_s and R_{ct}. Moreover, the presence of an almost vertical line in the low-frequency region, corresponding to the W, indicates effective ion diffusion throughout the porous framework of the material. Deviations from ideal capacitive behavior, particularly at low frequencies, are described by the CPE, which accounts for distributed capacitance arising from pore size variation and surface heterogeneity. For TPBZ-BTh and TPBZ-TTh CMPs, fitting the impedance spectra results in R_s values of 11.45 and 7.94 Ω and R_{ct} values of 9.0 and 7.3 Ω, respectively. The high capacitance of TPBZ-BTh and TPBZ-TTh CMPs is attributed to their good electrical conductivity and low internal resistance within the CMP framework, as evidenced by these low resistances, which also indicate strong electrode–electrolyte interactions and efficient ion transport pathways. While the increased impedance at higher frequencies indicates resistive constraints, the Bode magnitude plots

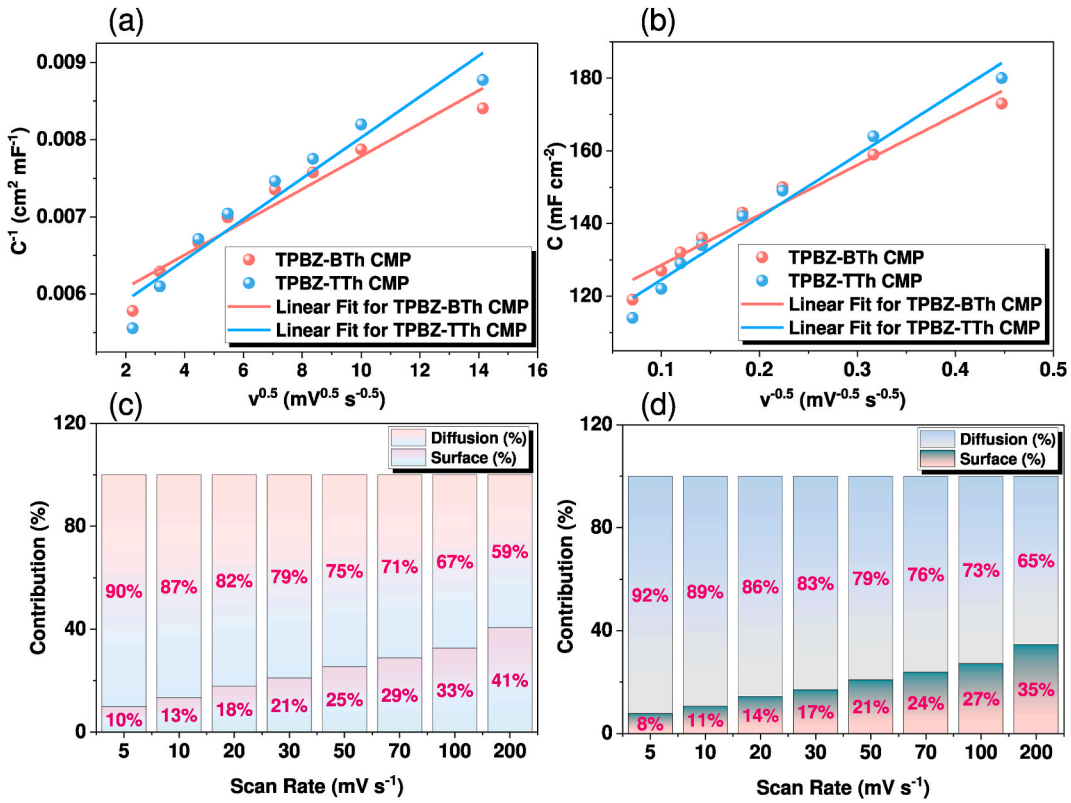

Fig. 6. (a) Plots of C^{-1} versus $v^{0.5}$. (b) Plots of the reciprocal of $v^{-0.5}$ vs areal capacitance (C). (c, d) Percentage contribution from EDLC and pseudocapacitance for (c) TPBZ-BTh and (d) TPBZ-TTh CMPs.

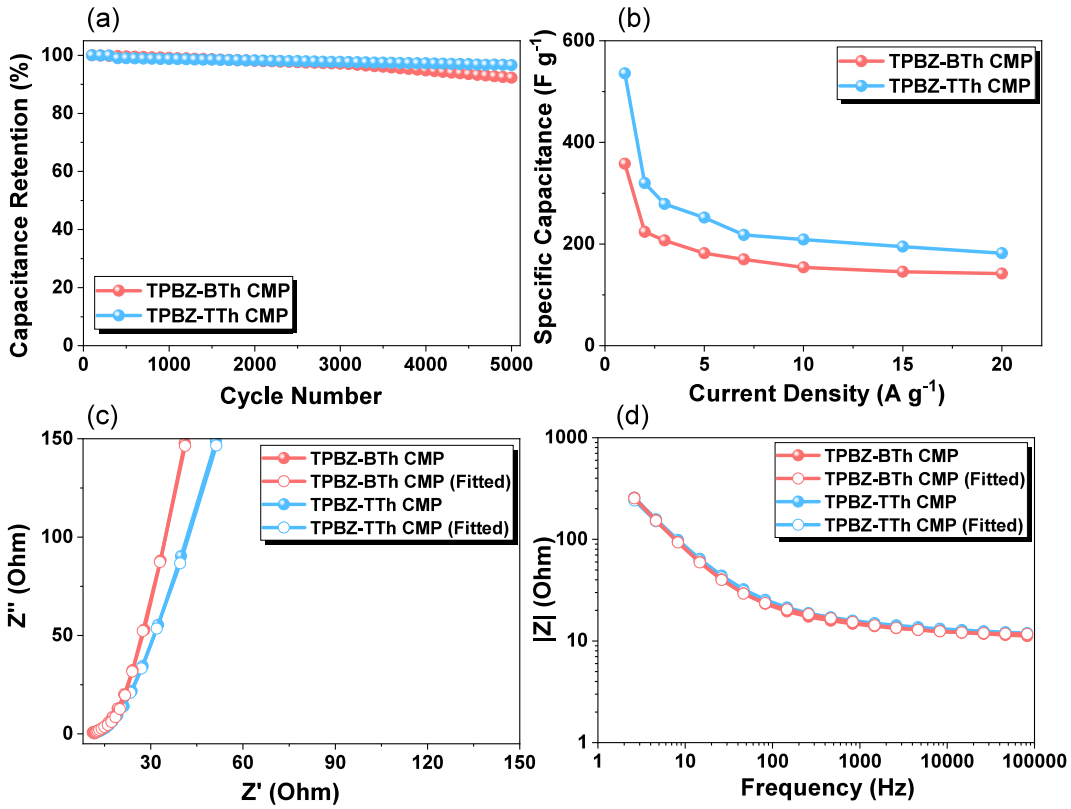

Fig. 7. (a) Percentage capacitance retention and (b) specific capacitance graphs of TPBZ-BTh and TPBZ-TTh CMPs for three three-electrode systems. (c) Nyquist plots and (d) Bode plot of frequency-dependent resistance (magnitude) for TPBZ-BTh and TPBZ-TTh CMPs.

[Fig. 7(d)] demonstrate a progressive reduction at lower frequencies, confirming capacitive behavior. The moderate knee frequencies indicate strong performance under high-rate operating conditions because they represent a well-balanced tradeoff between surface-controlled kinetics and ion diffusion. The XPS spectra of TPBZ-BTh CMP [Fig. S6(a)] and TPBZ-TTh CMP [Fig. S6(b)] after 5000 charge–discharge cycles exhibit characteristic C 1s peaks corresponding to C–C/C═C (284.13 eV), C═N (285.54 eV), C–N (286.82 eV), and C–S (287.95 eV). These results confirm that the π-conjugated CMP backbone remains structurally intact during prolonged electrochemical operation. Additional C 1s peaks at 289.16, 290.34, and 291.60 eV are attributed to the polymeric binder (Nafion), corresponding to C–SO_3, C–F, and CF_2 species, respectively. Following stability cycling, SEM observations of TPBZ-BTh CMP and TPBZ-TTh CMP [Fig. S7] indicate that the original morphological features are largely preserved relative to the pristine materials, despite noticeable increases in surface roughness and a more loosely packed particle arrangement. Portions of the larger aggregates are disintegrated into smaller granular domains, implying internal structural reorganization rather than actual material deterioration. The absence of pronounced collapse or severe fragmentation demonstrates the excellent morphological durability of the CMPs after prolonged electrochemical cycling.

3.3. *Electrochemical performance of TPBZ-BTh and TPBZ-TTh CMPs based on a symmetric coin cell*

The electrochemical performance of the symmetric SCs devices assembled from TPBZ-BTh CMP and TPBZ-TTh CMP electrodes (Fig. S8) was thoroughly investigated using GCD and CV techniques. All electrochemical tests were performed in a positive potential window of 0 to +0.8 V to evaluate the practical energy storage performance of the materials under symmetric two-electrode configurations. The CV profiles of the TPBZ-BTh and TPBZ-TTh CMPs symmetric devices [Fig. 8(a) and (b)] exhibited well-defined quasi-rectangular shapes, particularly at lesser scan rates, which are distinctive of an EDLC mechanism. The lack of distinct redox features suggests that charge storage is primarily controlled by electric double-layer adsorption at the electrode–electrolyte interface, while minor deviations from ideal rectangularity indicate a small pseudocapacitive contribution from heteroatoms (N and S) embedded in the conjugated framework. Importantly, both electrodes maintained highly stable electrochemical responses even under rapid scanning conditions, demonstrating their superior rate capability, fast ion transport, and outstanding structural integrity during rapid charge–discharge cycles. The GCD curves [Fig. 8(c) and (d)] of TPBZ-BTh and TPBZ-TTh CMPs devices further substantiated the CV results, displaying perfectly symmetrical triangular shapes with minimal voltage drop, confirming the dominant EDLC behavior and efficient charge–discharge reversibility.

Both CMP materials exhibited outstanding cycling stability, with TPBZ-BTh and TPBZ-TTh CMPs retaining 91.2% and 96.1% of their initial capacitance values, respectively, after 4000 consecutive charge–discharge cycles [Fig. 9(a)]. This excellent retention underscores the structural robustness and long-term electrochemical durability of the TPBZ-based CMP electrodes. At 1 A g^{-1}, the specific capacitances were calculated to be 176.4 F g^{-1} for TPBZ-BTh CMP and 207 F g^{-1} for TPBZ-TTh CMP, demonstrating the superior charge-storage capability of the TTh-based polymer. As the current density increased to 20 A g^{-1}, the specific capacitances gradually decreased to 59 and 67 F g^{-1}, respectively [Fig. 9(b)]. The capacitance drop at high current densities results from hindered ion diffusion, wherein electrolyte ions are unable to fully penetrate the microporous framework, limiting charge storage to the outer electrode's surface. At these higher rates, the shortened diffusion

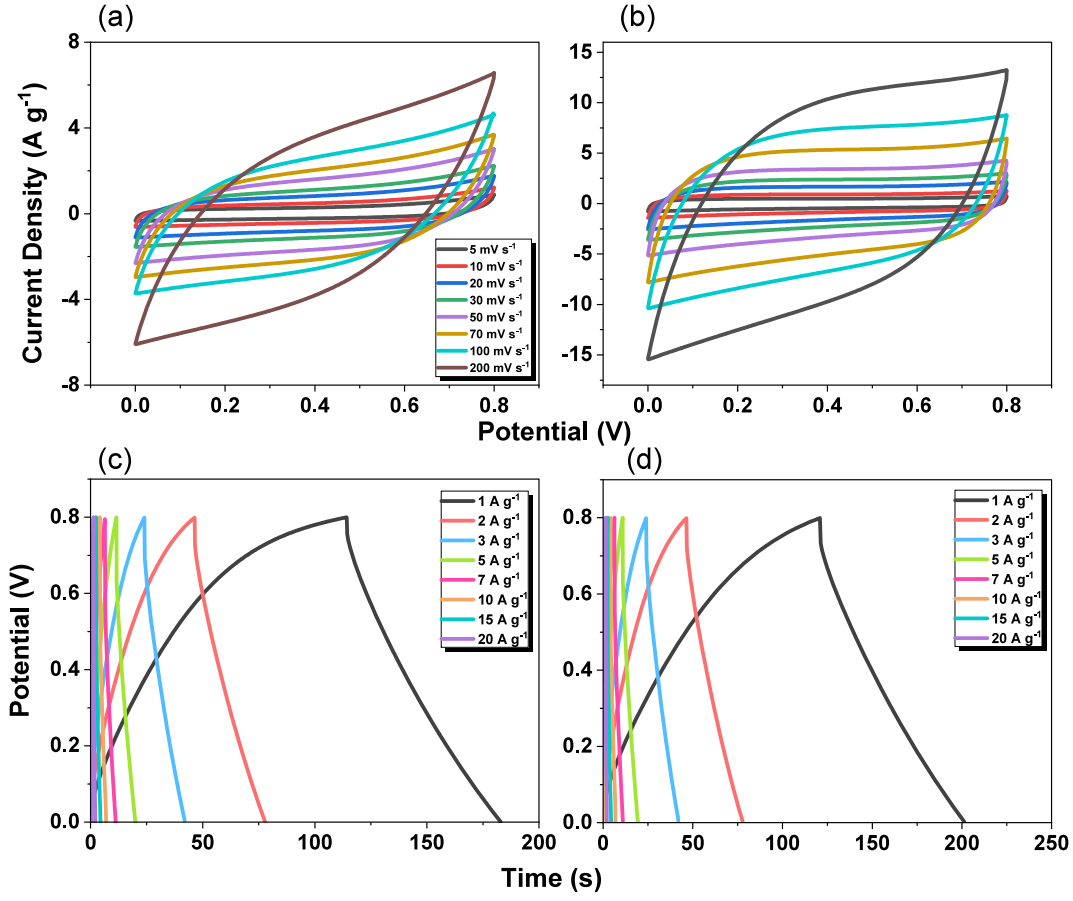

Fig. 8. (a, b) CV and (c, d) GCD curves of (a, c) TPBZ-BTh CMP and (b, d) TPBZ-TTh CMP, measured using a symmetric SCs coin cell.

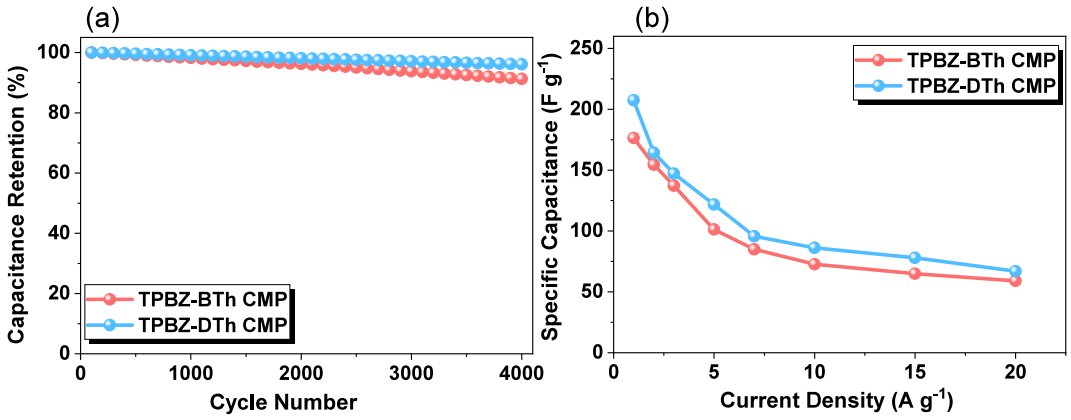

Fig. 9. (a) Percentage capacitance retention and (b) specific capacitance graphs of TPBZ-BTh and TPBZ-TTh CMPs for a symmetric coin cell.

time results in incomplete ion adsorption and desorption, thereby reducing effective capacitance. Notably, TPBZ-TTh CMP exhibited a significantly higher specific capacitance and superior cycling stability compared to its BTh analogue, TPBZ-BTh CMP. Although both CMPs possess extended π-conjugation and heteroatom-enriched frameworks favorable for charge storage, the TTh-based CMP demonstrates a more efficient electronic and electrochemical response. This enhancement arises from the electron-rich nature and highly conjugated planar geometry of the TTh moiety, which enables stronger π–electron delocalization and more effective charge transport along the polymer backbone. Furthermore, the unique spatial configuration of sulfur (S) atoms within the dithiophene unit promotes enhanced redox activity while simultaneously generating a more open and accessible porous network. This structural arrangement facilitates superior electrolyte infiltration, improved ion diffusion, and faster charge transfer kinetics throughout the electrode. The synergistic combination of these structural and electronic factors, including enhanced conjugation, optimized sulfur distribution, and increased pore accessibility, collectively leads to the significantly improved electrochemical performance of the TTh-based CMP, distinguishing it from its BTh counterpart.

To better understand the intrinsic charge-storage behavior and the underlying electrochemical mechanisms of the TPBZ-based electrodes,

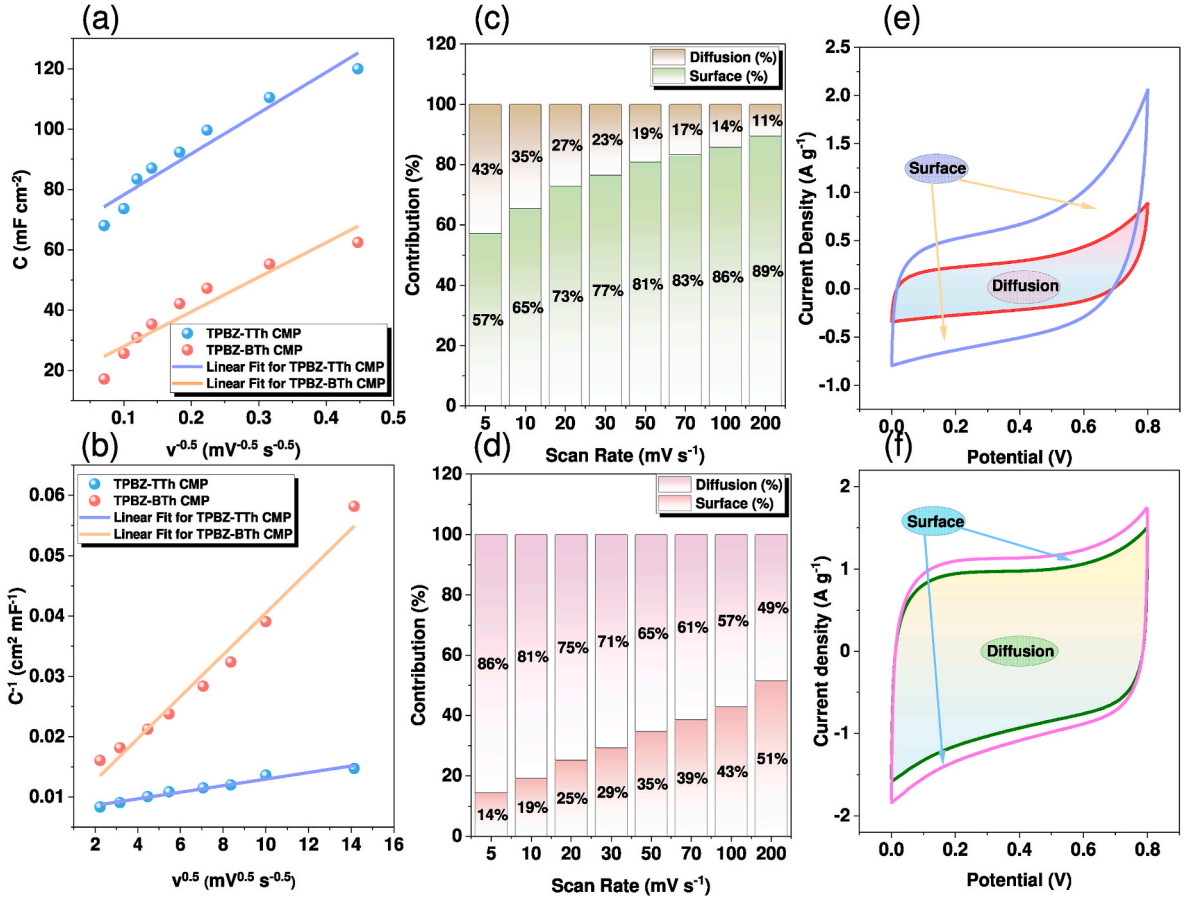

Fig. 10. (a) Plots of C against the reciprocal of $v^{-0.5}$. (b) Plots of the reciprocal of C^{-1} versus $v^{0.5}$. (c, d) Capacitance contribution from EDLC and pseudocapacitance for (c) TPBZ-BTh CMP and (d) TPBZ-TTh CMP (e, f) CV profile representing areal contribution of EDLC and pseudocapacitance at 5 mV s^{-1} for (e) TPBZ-BTh CMP and (f) TPBZ-TTh CMP.

Trasatti's method [55,56] was applied. This approach allows for a quantitative separation of the total capacitance into its diffusion-controlled (intercalation-type) and surface-controlled (capacitive) components. The areal capacitance (C) values were derived from CV data collected at various scan rates, yielding 62.4 mF cm^{-2} for TPBZ-BTh CMP and 120 mF cm^{-2} for TPBZ-TTh CMP [Fig. S9], demonstrating the superior charge-storage capacity of the TTh-based CMP. A plot of $v^{1/2}$ vs the reciprocal of C^{-1} exhibited a direct relationship [Fig. 10(a) and (b)], signifying a semi-infinite ion diffusion process occurring within the porous electrode frameworks. A complementary plot of areal capacitance versus $v^{1/2}$ also produced a linear trend, consistent with the supposition of semi-infinite diffusion of ions within the microporous structure. From this relationship, the total capacitance (C_t) and relative distribution of diffusion- and surface-controlled processes were calculated. At 5 mV s^{-1}, the EDLC (surface-controlled) contribution was determined to be 57% for TPBZ-BTh CMP and only 14% for TPBZ-TTh CMP, as shown in Fig. 10(c) and (d).

The corresponding CV profiles at 5 mV s^{-1} [Fig. 10(e) and (f)] reveal that the shaded regions represent the portion of capacitance arising from diffusion-controlled processes, which dominate at lower scan rates. Specifically, TPBZ-TTh and TPBZ-BTh CMPs exhibited diffusion-controlled contributions of 86% and 43%, respectively. The diffusion-controlled process's contribution gradually declined as the scan rate increased, falling to 49% for TPBZ-TTh CMP and 11% for TPBZ-BTh CMP at 200 mV s^{-1}. This decline reflects the reduced ion diffusion efficiency at increased scan rates, where the incomplete time available for electrolyte ions to penetrate the inner micropores confines charge storage primarily to the electrode surface. Such behavior is typical of porous and conjugated electrode materials, highlighting the delicate interplay between ion transport kinetics, electrode architecture, and charge-storage dynamics [57,58]. The distinctive structure of these CMPs, characterized by amorphous frameworks and rich in N and S heteroatoms, establishes a synergistic environment that facilitates efficient ion transport, enhances electrical conductivity, and boosts overall capacitance performance. The coexistence of diffusion-controlled redox reactions and surface-driven double-layer formation further accounts for their superior electrochemical characteristics. A Ragone plot, depicting correlation among energy and power densities, is an essential analytical tool used to assess the balance between energy storage capacity and power delivery capability in energy storage systems. As shown in Fig. 11 (a), the TPBZ-TTh CMP symmetric device exhibited an exceptionally extraordinary energy density of 36.1 Wh kg^{-1} at a power density of 1591.5 W kg^{-1}, reflecting its outstanding charge-storage capability under moderate discharge conditions. Remarkably, even at a very high-power density of 54900 W kg^{-1}, the device retained a substantial energy density of 12.2 Wh kg^{-1}, underscoring its excellent rate performance and quick charge–discharge capability. In comparison, the TPBZ-BTh CMP-based symmetric device achieved a supreme energy density of 32.1 Wh kg^{-1} at a power density of 1681.3 W kg^{-1}, which, while slightly lower than that of TPBZ-TTh CMP, still indicates a robust energy storage behavior and efficient electrochemical reversibility. These results clearly demonstrate that the TPBZ-TTh CMP outperforms its BTh counterpart, primarily due to its higher surface area, optimized pore structure, and enhanced charge transport efficiency derived from the electron-rich TTh framework. Overall, both TPBZ-BTh and TPBZ-TTh CMPs exhibit outstanding power-handling characteristics, making them highly suitable for applications requiring rapid energy delivery and fast charge–discharge processes, such as in high-power supercapacitors and hybrid energy storage systems. Furthermore, the comparative Ragone analysis [Fig. 11(b)] highlights the competitive performance of these TPBZ-based CMPs relative to other reported materials in the literature [59–65], confirming their potential as next-generation, high-performance, and sustainable electrode materials for advanced energy storage technologies. Ultimately, the data presented in Table S3 and S4 demonstrate that TPBZ-TTh CMP delivers exceptional supercapacitive (SC) performance in both three-electrode and two-electrode systems, surpassing many previously reported electrode materials. This outstanding behavior underscores the superior electrochemical efficiency and well-designed structural features of TPBZ-TTh CMP.

Density functional theory (DFT) calculations were performed to elucidate the electronic structures of the TPBZ-TTh and TPBZ-BTh CMPs [Fig. 12]. All DFT calculations were carried out at the B3LYP/6-31G* level. Recent studies on DFT-guided design of CMPs for SCs have demonstrated that narrow bandgaps and efficient orbital delocalization are crucial for enhancing electrical conductivity and improving rate capability [66,67]. In this context, TPBZ-TTh CMP, the highest occupied molecular orbital (HOMO) is predominantly localized on the TTh units, while the lowest unoccupied molecular orbital (LUMO) is mainly distributed over the TPBZ units with a minor contribution from the TTh moieties. This distinct spatial separation of frontier orbitals facilitates efficient intramolecular charge transfer and promotes rapid electron transport along the polymer backbone, which is advantageous for achieving low internal resistance and high-power density in supercapacitor electrodes. In contrast, TPBZ-BTh CMP exhibits a more delocalized HOMO extending across both TPBZ and BTh units, whereas the LUMO is primarily localized on the TPBZ units with partial contribution from one thiophene unit of BTh. In addition, the deeper-lying occupied orbitals (HOMO−2 and HOMO−3) are mainly localized on the BTh units with limited extension onto the TPBZ [Fig. S10]. Given the established structure-property relationships in energy storage materials, such partial spatial overlap between occupied and unoccupied orbitals may induce localized charge trapping and increase internal charge recombination, thereby limiting charge transport efficiency and rate performance in

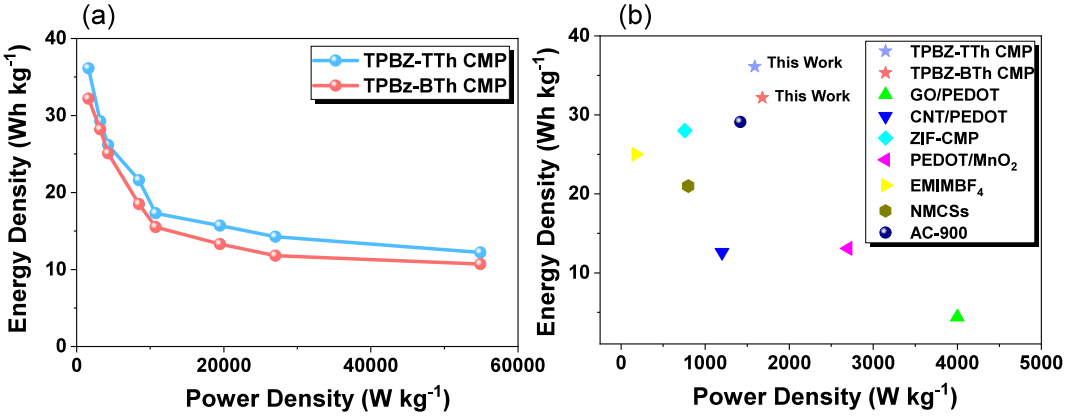

Fig. 11. (a) Ragone plots of TPBZ-BTh and TPBZ-TTh CMPs, showing energy density (Wh kg^{-1}) as a function of power density (W kg^{-1}). (b) Comparison of the energy densities of TPBZ-BTh and TPBZ-TTh CMPs with representative literature-reported materials supercapacitors.

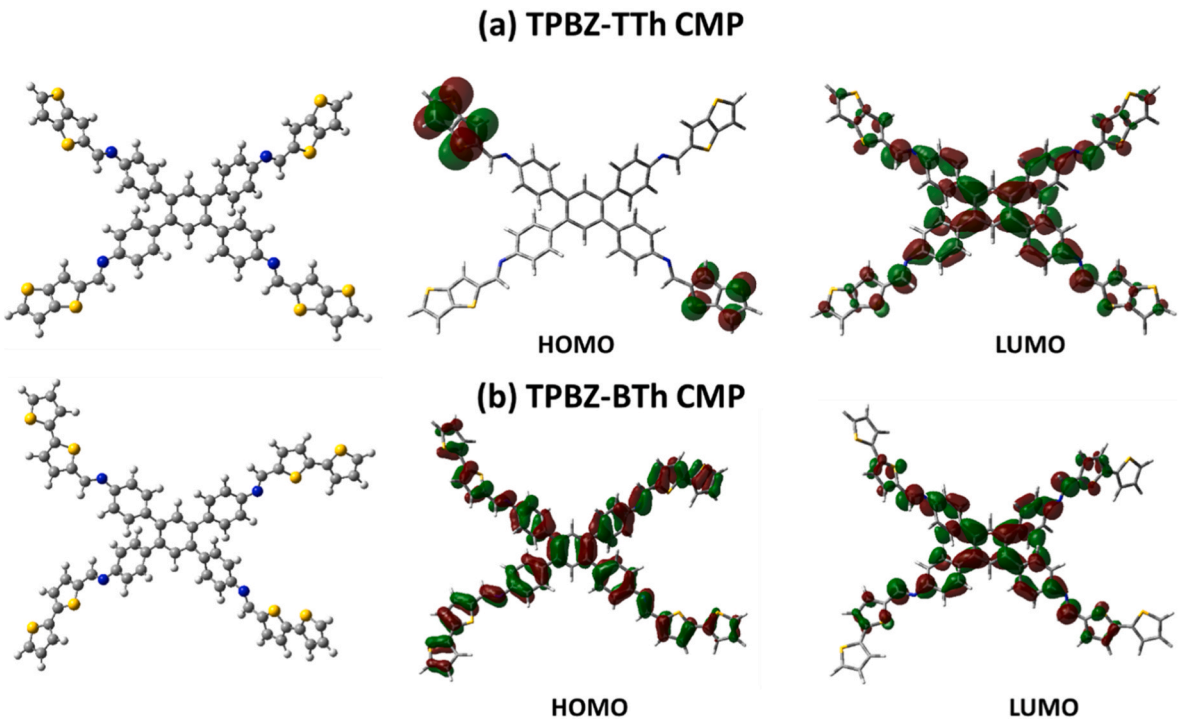

Fig. 12. The HOMO and LUMO orbitals of (a) TPBZ-TTh CMP and (b) TPBZ-BTh CMP.

electrochemical energy storage applications. The calculated frontier molecular orbital energies further support these interpretations. TPBZ-TTh CMP exhibits HOMO and LUMO energy levels of −7.98 and −6.84 eV, respectively, corresponding to a relatively narrow bandgap of 1.13 eV, which is favorable for enhanced electronic conductivity and rapid charge transfer during repeated charge–discharge processes. In comparison, TPBZ-TTh CMP shows a deeper HOMO and a comparable LUMO level (−8.73 and −6.79 eV), resulting in a larger bandgap of 1.94 eV that may hinder charge delocalization and reduce electrical conductivity.

4. Conclusions

Using the Schiff-base condensation route [4 + 2], two CMPs, TPBZ-BTh and TPBZ-TTh, were successfully synthesized. The electrochemical performances of both TPBZ-BTh and TPBZ-TTh CMPs were systematically evaluated through GCD and CV measurements. Among the two TPBZ-CMPs, TPBZ-TTh CMP exhibited markedly superior electrochemical behavior, attaining an explicit capacitance of 536 F g^{-1} compared to 358 F g^{-1} for TPBZ-BTh CMP at a 1 A g^{-1}. To assess their practical potential, symmetric supercapacitor devices were assembled using each material as an active electrode. The TPBZ-TTh CMP-based symmetric device conveyed a remarkable capacitance of 207 F g^{-1}, outperforming the TPBZ-BTh CMP, which reached 176.4 F g^{-1} at the same current density. Both CMPs demonstrated remarkable cycling stability, maintaining 92.1% (TPBZ-TTh CMP) and 96.2% (TPBZ-BTh CMP) of their initial capacitance after 4000 charge–discharge cycles. Overall, this study highlights a molecular-level design strategy for tailoring the electronic architecture of thiophene-based CMPs to achieve high-performance supercapacitor energy storage.

CRediT authorship contribution statement

Mohamed Gamal Mohamed: Writing – review & editing, Writing – original draft, Supervision, Methodology, Investigation, Formal analysis, Data curation, Conceptualization. **Abdul Basit:** Writing – original draft, Formal analysis, Data curation. **Ahmed A.K. Mohammed:** Software. **Shiao-Wei Kuo:** Supervision, Resources, Project administration, Funding acquisition.

Declaration of competing interest

The authors declare that they have no known competing financial interests or personal relationships that could have appeared to influence the work reported in this paper.

Acknowledgments

This study was supported financially by the National Science and Technology Council, Taiwan, under contracts NSTC 114-2223-E-110-001- and 113-2221-E-110-012-MY3. The authors thank the staff at National Sun Yat-sen University for their assistance with the TEM (ID: EM022600) experiments.

Appendix A. Supplementary data

Supplementary data to this article can be found online at https://doi.org/10.1016/j.mtchem.2026.103492.

Data availability

Data will be made available on request.

References

[1] W. Lyu, W. Zhang, H. Liu, Y. Liu, H. Zuo, C. Yan, C.F.J. Faul, A. Thomas, M. Zhu, Y. Liao, Conjugated microporous polymer network grafted carbon nanotube fibers with tunable redox activity for efficient flexible wearable energy storage, Chem. Mater. 32 (2020) 8276–8285, https://doi.org/10.1021/acs.chemmater.0c02089.
[2] F. Al Mubarak, R. Rezaee, D.A. Wood, Economic, societal, and environmental impacts of available energy sources: a review, Eng 5 (2024) 1232–1265, https://doi.org/10.3390/eng5030067.
[3] R.M. Elavarasan, The motivation for renewable energy and its comparison with other energy sources: a review, Eur. J. Sustain. Dev. Res. 3 (2019) em0076, https://doi.org/10.20897/ejosdr/4005.

[4] S. Lorek, J.H. Spangenberg, Sustainable consumption within a sustainable economy–beyond green growth and green economies, J. Clean. Prod. 63 (2014) 33–44, https://doi.org/10.1016/j.jclepro.2013.08.045.

[5] K. Kaygusuz, Energy for sustainable development: a case of developing countries, Renew. Sustain. Energy Rev. 16 (2012) 1116–1126, https://doi.org/10.1016/j.rser.2011.11.013.

[6] M. Pathak, D. Bhatt, R.C. Bhatt, B.S. Bohra, G. Tatrari, S. Rana, M.C. Arya, N. G. Sahoo, High energy density supercapacitors: an overview of efficient electrode materials, electrolytes, design, and fabrication, Chem. Rec. 24 (2024) e202300236, https://doi.org/10.1002/tcr.202300236.

[7] J. Yan, Q. Wang, T. Wei, Z. Fan, Recent advances in design and fabrication of electrochemical supercapacitors with high energy densities, Adv. Energy Mater. 4 (2014) 1300816, https://doi.org/10.1002/aenm.201300816.

[8] M. Winter, R.J. Brodd, What are batteries, fuel cells, and supercapacitors? Chem. Rev. 104 (2004) 4245–4270, https://doi.org/10.1021/cr020730k.

[9] X. Zhao, B.M. Sánchez, P.J. Dobson, P.S. Grant, The role of nanomaterials in redox-based supercapacitors for next generation energy storage devices, Nanoscale 3 (2011) 839–855, https://doi.org/10.1039/C0NR00594K.

[10] G.G. Njema, R.B.O. Ouma, J.K. Kibet, A review on the recent advances in battery development and energy storage technologies, J. Renew. Energy 1 (2024) 2329261, https://doi.org/10.1155/2024/2329261.

[11] A.K. Tareen, K. Khan, M. Iqbal, Y. Zhang, J. Long, F. Nazeer, A. Mahmood, N. Mahmood, Z. Shi, C. Ma, W. Huan, M.F. Khan, J. Yin, C. Li, H. Zhang, Recent advances in novel graphene: new horizons in renewable energy storage technologies, J. Mater. Chem. C 10 (2022) 11472–11531, https://doi.org/10.1039/D2TC02233H.

[12] Z. Zhang, X. Wang, X. Li, J. Zhao, G. Liu, W. Yu, X. Dong, J. Wang, Review on composite solid electrolytes for solid-state lithium-ion batteries, Mater. Today Sustain. 21 (2023) 100316, https://doi.org/10.1016/j.mtsust.2023.100316.

[13] M.G.M. Abdolrasol, S. Ansari, I.A. Sarker, S.K. Tiong, M.A. Hannan, Lithium-ion to sodium-ion batteries transitioning: trends, analysis and innovative technologies prospects in EV application, Prog. Energy 7 (2025) 022007, https://doi.org/10.1088/2516-1083/adbff0.

[14] A. Mohanty, S. Sahu, L.B. Sukla, N. Devi, Application of various processes to recycle lithium-ion batteries (LIBs): a brief review, Mater. Today Proc. 47 (2021) 1203–1212, https://doi.org/10.1016/j.matpr.2021.03.645.

[15] J. Yu, N. Li, H.G. Wang, B. Gao, B. Wang, Z. Li, Unraveling the superior anodic lithium storage behavior in the redox-active porphyrinic triazine frameworks, Chem. Eng. J. 463 (2023) 142434, https://doi.org/10.1016/j.cej.2023.142434.

[16] H.G. Wang, Y. Wang, Q. Wu, G. Zhu, Recent developments in electrode materials for dual-ion batteries: potential alternatives to conventional batteries, Mater. Today 52 (2022) 269, https://doi.org/10.1016/j.mattod.2021.11.008.

[17] H. Li, F. Pan, C. Qin, T. Wang, K.J. Chen, Porous organic polymers-based single-atom catalysts for sustainable energy-related electrocatalysis, Adv. Energy Mater. 13 (2023) 2301378, https://doi.org/10.1002/aenm.202301378.

[18] X. Liu, C.F. Liu, W.Y. Lai, W. Huang, Porous organic polymers as promising electrode materials for energy storage devices, Adv. Mater. Technol. 5 (2020) 2000154, https://doi.org/10.1002/admt.202000154.

[19] T. Zhang, V.G. Gregoriou, N. Gasparini, C.L. Chochos, Porous organic polymers in solar cells, Chem. Soc. Rev. 51 (2022) 4465–4483, https://doi.org/10.1039/D2CS00123C.

[20] M.G. Mohamed, B.X. Su, S.W. Kuo, Robust nitrogen-doped microporous carbon via crown ether-functionalized benzoxazine-linked porous organic polymers for enhanced CO2 adsorption and supercapacitor applications, ACS Appl. Mater. Interfaces 16 (2024) 40858–40872, https://doi.org/10.1021/acsami.4c05645.

[21] D.H. Yang, Y. Tao, X. Ding, B.H. Han, Porous organic polymers for electrocatalysis, Chem. Soc. Rev. 51 (2022) 761–791, https://doi.org/10.1039/D1CS00887K.

[22] K.S. Song, P.W. Fritz, A. Coskun, Porous organic polymers for CO2 capture, separation and conversion, Chem. Soc. Rev. 51 (2022) 9831–9852, https://doi.org/10.1039/D2CS00727D.

[23] J. Yu, X. Zhang, Y. Liu, L. Cheng, H.G. Wang, F. Cui, G. Zhu, Donor–acceptor porous aromatic framework cathode with fast redox kinetics for ultralow-temperature (−70 °C) potassium-organic batteries, Angew. Chem. Int. Ed. 64 (2025) e202507570, https://doi.org/10.1002/anie.202507570.

[24] Z. Zhang, J. Jia, Y. Zhi, S. Ma, X. Liu, Porous organic polymers for light-driven organic transformations, Chem. Soc. Rev. 51 (2022) 2444–2490, https://doi.org/10.1039/D1CS00808K.

[25] W. He, J. Li, S. Chen, Y. Deng, S. Li, C.F.J. Faul, Y. Liao, Controllable porosities of conjugated microporous polytriphenylamine enable high sensitivity toward trimethylamine at low temperatures, Sci. China Mater. 68 (2025) 1592–1601, https://doi.org/10.1007/s40843-024-3298-0.

[26] Y. Li, J. Duan, Y. Wang, L. Teng, H. Liu, J. Li, M. Liu, W. He, H. Hu, L. Wang, W. Lyu, Y. Liao, Cu-mediated bipolar-type extended π-conjugated microporous polymers for lithium-ion battery cathodes with high energy density and fast-charging capability, Chem. Sci. 16 (2025) 11311–11321, https://doi.org/10.1039/D4SC08244C.

[27] X. Liu, C.F. Liu, S. Xu, T. Cheng, S. Wang, W.Y. Lai, W. Huang, Porous organic polymers for high-performance supercapacitors, Chem. Soc. Rev. 51 (2022) 3181–3225, https://doi.org/10.1039/D2CS00065B.

[28] S. Fajal, S. Dutta, S.K. Ghosh, Porous organic polymers (POPs) for environmental remediation, Mater. Horiz. 10 (2023) 4083–4138, https://doi.org/10.1039/D3MH00672G.

[29] X. Mi, J. Li, W. Lyu, L. Xu, Y. Liu, C. Qian, J. Yu, W. He, J. Feng, Y. Liao, Boosting Fenton-like reaction via enhanced charge transfer in donor-acceptor polyaniline-like conjugated microporous polymers, Appl. Catal. B Environ. Energy 378 (2025) 125530, https://doi.org/10.1016/j.apcatb.2025.125530.

[30] B. Zheng, X. Lin, X. Zhang, D. Wu, K. Matyjaszewski, Emerging functional porous polymeric and carbonaceous materials for environmental treatment and energy storage, Adv. Func. Mater. 30 (2020) 1907006, https://doi.org/10.1002/adfm.201907006.

[31] T.X. Wang, H.P. Liang, D.A. Anito, X. Ding, B.H. Han, Emerging applications of porous organic polymers in visible-light photocatalysis, J. Mater. Chem. A 8 (2020) 7003–7034, https://doi.org/10.1039/D0TA00364F.

[32] T. Zhang, G. Xing, W. Chen, L. Chen, Porous organic polymers: a promising platform for efficient photocatalysis, Mater. Chem. Front. 4 (2020) 332–353, https://doi.org/10.1039/C9QM00633H.

[33] M.G. Suarez, Y. Chen, J. Zhang, Porous organic polymers as a promising platform for efficient capture of heavy metal pollutants in wastewater, Polym. Chem. 14 (2023) 4000–4032, https://doi.org/10.1039/D3PY00632H.

[34] A. Basit, Y.C. Kao, Y.A. El-Ossaily, S.W. Kuo, M.G. Mohamed, Rational engineering and synthesis of pyrene and thiazolo[5,4-d]thiazole-functionalized conjugated microporous polymers for efficient supercapacitor energy storage, J. Mater. Chem. A 12 (2024) 30508–30521, https://doi.org/10.1039/D4TA05908E.

[35] H. Ma, Y. Chen, X. Li, B. Li, Advanced applications and challenges of electropolymerized conjugated microporous polymer films, Adv. Func. Mater. 31 (2021) 2101861, https://doi.org/10.1002/adfm.202101861.

[36] S. Feng, H. Cheng, F. Chen, X. Liu, Z. Wang, H. Xu, J. Hua, Rational design of covalent organic frameworks with redox-active catechol moieties for high-performance overall photosynthesis of hydrogen peroxide, ACS Catal. 14 (2024) 7736–7745, https://doi.org/10.1021/acscatal.4c01411.

[37] Z. Xu, Q. Duan, X. Cui, Copper-porphyrin-based covalent organic frameworks for efficient water remediation: a synergistic strategy of adsorption and photo-self-fenton degradation, Chem. Eng. J. 511 (2025) 162241, https://doi.org/10.1016/j.cej.2025.162241.

[38] L. Li, C. Zhao, H. Wang, Recent progress in synthesis and application of thiophene oligomers based on bithiophene dicarbanions, Chem. Rec. 16 (2016) 797–809, https://doi.org/10.1002/tcr.201500270.

[39] X. Pan, W. Xiong, T. Liu, X. Sun, L. Huo, D. Wei, M. Yu, M. Han, Y. Sun, Influence of 2,2-bithiophene and thieno[3,2-b] thiophene units on the photovoltaic performance of benzodithiophene-based wide-bandgap polymers, J. Mater. Chem. C 5 (2017) 4471–4479, https://doi.org/10.1039/C7TC00720E.

[40] C.Y. Kuo, W. Nie, H. Tsai, H.J. Yen, A.D. Mohite, G. Gupta, A.M. Dattelbaum, D. J. William, K.C. Cha, Y. Yang, L. Wang, H.L. Wang, Structural design of benzo[1,2-b:4,5-b′]dithiophene-based 2D conjugated polymers with bithienyl and terthienyl substituents toward photovoltaic applications, Macromolecules 47 (2014) 1008–1020, https://doi.org/10.1021/ma401846n.

[41] D.S. Chung, J.W. Park, S.O. Kim, K. Heo, C.E. Park, M. Ree, Y.H. Kim, S.K. Kwon, Alternating copolymers containing bithiophene and dialkoxynaphthalene for the applications to field effect transistor and photovoltaic cell: performance and stability, Chem. Mater. 21 (2009) 5499–5507, https://doi.org/10.1021/cm9025057.

[42] D. Patra, M. Comí, X. Zhang, G.P. Kini, M. Udayakantha, A.J. Kalin, S. Banerjee, L. Fang, X. Guo, M. Al-Hashimi, Design, synthesis and characterization of fused bithiazole- and dithiophene-based low bandgap thienylenevinylene copolymers, Polym. Chem. 12 (2021) 5942–5951, https://doi.org/10.1039/D1PY00773D.

[43] S. Ming, S. Zhen, H. Zhang, Z. Zhang, B. Lu, J. Zhao, G. Nie, J. Xu, Solvent-soluble thiophene-benzene based electrochromic polymers as electrode materials for supercapacitor, Polymer 267 (2023) 125675, https://doi.org/10.1016/j.polymer.2023.125675.

[44] D. Xiao, B. Sun, Y. Liu, E. Jiao, X. Wang, X. Chen, X. Cheng, K. Guo, K. Yuan, H. Zhang, Development status of supercapacitors and their widely applied organic semiconductors: polythiophene conjugated polymers, Polym. Polym. Compos. 33 (2025) 1–19, https://doi.org/10.1177/09673911241304848.

[45] M.G. Mohamed, A. Basit, C.Y. Shih, S.U. Sharma, T. Mondal, S.W. Kuo, Pyrene-linked covalent organic polymer/single-walled carbon nanotubes hybrids as high-performance electrodes for supercapacitive energy storage, ACS Appl. Energy Mater. 8 (2025) 3764–3778, https://doi.org/10.1021/acsaem.5c00052.

[46] L. Wang, J. Liu, J. Wang, J. Huang, Bifunctional thiophene-based covalent organic frameworks for Hg^{2+} removal and I_2 vapor adsorption, Chem. Eng. J. 473 (2023) 145405, https://doi.org/10.1016/j.cej.2023.145405.

[47] Q. Zhang, C. Liang, Z. Wang, X. Wang, Thieno[3,2-b]thiophene-containing conjugated microporous polymer–derived sulfur-doped hard carbon for enhanced lithium storage, Ionics 31 (2025) 4373–4382, https://doi.org/10.1007/s11581-025-06171-x.

[48] Q. Huang, L. Guo, N. Wang, X. Zhu, S. Jin, B. Tan, Layered thiazolo [5,4-d] thiazole-linked conjugated microporous polymers with heteroatom adoption for efficient photocatalysis application, ACS Appl. Mater. Interfaces 11 (2019) 15861–15868, https://doi.org/10.1021/acsami.8b21765.

[49] Y. Luo, Z. Yan, F. Wang, Z. Wang, M. Zhou, Y. Jin, Y. Wang, C. Xia, 3D ultra-micropore organic polymers with fixed group and thieno[3,2-b]thiophene to enhance adsorption and separation of Xe/Kr, Sep. Purif. Technol. 330 (2024) 125460, https://doi.org/10.1016/j.seppur.2023.125460.

[50] A. Basit, M.G. Mohamed, H. Karim, S.W. Kuo, Synergistic engineering of anthracene and thiazolo[5,4-d] thiazole–based donor–acceptor conjugated microporous polymers with heteroatom adoption for enhanced energy storage capacity, J. Mater. Chem. A 13 (2025) 41913–41930, https://doi.org/10.1039/D5TA05442G.

[51] W. Lu, L. Yan, W. Ye, J. Ning, Y. Zhong, Y. Hu, Defect engineering of electrode materials towards superior reaction kinetics for high-performance supercapacitors, J. Mater. Chem. A 10 (2022) 15267–15296, https://doi.org/10.1039/D2TA02930H.

[52] P. Bhojane, Recent advances and fundamentals of pseudocapacitors: materials, mechanism, and its understanding, J. Energy Storage 45 (2022) 103654, https://doi.org/10.1016/j.est.2021.103654.
[53] G.Z. Chen, Linear and non-linear pseudocapacitances with or without diffusion control, Prog. Natl. Sci. Mat. Int. 31 (2021) 792–800, https://doi.org/10.1016/j.pnsc.2021.10.011.
[54] L.J. Sun, X.Y. Zhang, C. Bai, H.L. Guo, C.M. Han, Y.F. Zhang, H.M. Hu, Cobalt/nickel 2D MOF nanosheets with a bithiophene-tetraterpyridyl derivative ligand for high-performance supercapacitors through boosting pseudocapacitance, J. Energy Storage 92 (2024) 112197, https://doi.org/10.1016/j.est.2024.112197.
[55] M.G. Mohamed, C.C. Chen, M. Ibrahim, A.O. Mousa, M.H. Elsayed, Y. Ye, S.W. Kuo, Tetraphenylanthraquinone and dihydroxybenzene-tethered conjugated microporous polymer for enhanced CO_2 uptake and supercapacitive energy storage, JACS Au 4 (2024) 3593–3605, https://doi.org/10.1021/jacsau.4c00537.
[56] R. Anjana, P. Anjana, J. Alex, R. Isaac, R.S. Hussain, D. Sajan, Investigations on supercapacitor performance of novel ZnO-CeO2-rGO nanohybrid prepared via hydrothermal method for energy storage applications and their charge storage mechanism, Diam. Relat. Mater. 146 (2024) 111241, https://doi.org/10.1016/j.diamond.2024.111241.
[57] M.M. Samy, M.G. Mohamed, S.U. Sharma, S.V. Chaganti, J.T. Lee, S.W. Kuo, An ultrastable tetrabenzonaphthalene-linked conjugated microporous polymer functioning as a high-performance electrode for supercapacitors, J. Taiwan Inst. Chem. Eng. 158 (2024) 104750, https://doi.org/10.1016/j.jtice.2023.104750.
[58] T. Yang, C. Zhang, W. Ma, X. Gao, C. Yan, F. Wang, J.X. Jiang, Thiophene-rich conjugated microporous polymers as anode materials for high performance lithium- and sodium-ion batteries, Solid State Ionics 347 (2020) 115247, https://doi.org/10.1016/j.ssi.2020.115247.
[59] S. Ahmed, A. Ahmed, M. Rafat, Supercapacitor performance of activated carbon derived from rotten carrot in aqueous, organic and ionic liquid-based electrolytes, J. Saudi Chem. Soc. 22 (2018) 993–1002, https://doi.org/10.1016/j.jscs.2018.03.002.
[60] Z. Liang, H. Liu, J. Zeng, J. Zhou, H. Li, H. Xia, Facile synthesis of nitrogen-doped microporous carbon spheres for high performance symmetric supercapacitors, Nanoscale Res. Lett. 13 (2018) 314, https://doi.org/10.1186/s11671-018-2713-0.
[61] M. Karnan, K. Subramani, P.K. Srividhya, M. Sathish, Electrochemical studies on corncob derived activated porous carbon for supercapacitors application in aqueous and non-aqueous electrolytes, Electrochim. Acta 228 (2017) 586–596, https://doi.org/10.1016/j.electacta.2017.01.095.
[62] M.D. Merrill, E. Montalvo, P.G. Campbell, Y.M. Wang, M. Stadermann, T. F. Baumann, J. Biener, M.A. Worsley, Optimizing supercapacitor electrode density: achieving the energy of organic electrolytes with the power of aqueous electrolytes, RSC Adv. 4 (2014) 42942–42946, https://doi.org/10.1039/C4RA08114E.
[63] X. He, W. Yang, X. Mao, L. Xu, Y. Zhou, Y. Chen, Y. Zhao, Y. Yang, J. Xu, All-solid state symmetric supercapacitors based on compressible and flexible free-standing 3D carbon nanotubes (CNTs)/poly(3,4-ethylenedioxythiophene) (PEDOT) sponge electrodes, J. Power Sources 376 (2018) 138–146, https://doi.org/10.1016/j.jpowsour.2017.09.084.
[64] H. Zhou, H.J. Zhai, G. Han, Superior performance of highly flexible solid-state supercapacitor based on the ternary composites of graphene oxide supported poly (3,4-ethylenedioxythiophene)-carbon nanotubes, J. Power Sources 323 (2016) 125–133, https://doi.org/10.1016/j.jpowsour.2016.05.049.
[65] J. Gong, Z. Xu, Z. Tang, J. Zhong, L. Zhang, Highly compressible 3-D hierarchical porous carbon nanotube/metal organic framework/polyaniline hybrid sponges supercapacitors, AIP Adv. 9 (2019) 055032, https://doi.org/10.1063/1.5109042.
[66] A.D. Savariraj, P.M. Austeria, P.J. Jesuraj, P. Vinothbabu, P. Sivakumar, J. James, H. Jung, Electron delocalization and gradient orbital hybridization to enhance charge kinetics in interfacial heterostructure toward efficient energy storage, Mater. Today Phys. 59 (2025) 101908, https://doi.org/10.1016/j.mtphys.2025.101908.
[67] M. Özdemir, S. Uluçay, E. Sevimli, S. Altınışık, B. Köksoy, B. Yalçın, S. Koyuncu, Light-induced performance enhancement of supercapacitors through thiol–ene click surface functionalization of thienothiophene-BODIPY porous polymers, ACS Appl. Energy Mater. 8 (2025) 17232–17245, https://doi.org/10.1021/acsaem.5c02377.